INORGANIC CHEMISTRY
FRONTIERS

RESEARCH ARTICLE

View Article Online
View Journal | View Issue

Cite this: *Inorg. Chem. Front.*, 2024, **11**, 8679

Tunable luminescence *via* Cr^{3+}–Yb^{3+}/Nd^{3+} energy transfer in Cr^{3+} and Yb^{3+}/Nd^{3+} coactivated NIR phosphors for non-destructive analysis†

Xiaowei Zhang,[a,b] Dashuai Sun,[b] Pengcheng Luo,[b] Luhui Zhou,[b] Zheng Lu,[b] Jia Liu,[b] Congcong Fan,[b] Xinyu Ye *[a] and Hongpeng You *[b]

Received 6th September 2024,
Accepted 29th October 2024

DOI: 10.1039/d4qi02260b

rsc.li/frontiers-inorganic

For efficient near-infrared (NIR) emitters, tuning their luminescence properties is important for their extended optical applications. A fundamental study of garnet-type inorganics has led to the development of a new NIR phosphor $Y_3ScAl_4O_{12}:Cr^{3+}$ (YSAO:Cr^{3+}), exhibiting emission in the range of 600 to 950 nm, an internal quantum efficiency (IQE) of 84.01%, and good thermal stability at 423 K (89.7% of that at room temperature). Doping with Yb^{3+}/Nd^{3+} ions helps achieve an efficient energy transfer from the Cr^{3+} to Yb^{3+}/Nd^{3+} ions with excellent thermal stability. NIR pc-LED devices prepared using YSAO:Cr^{3+},Yb^{3+} and YSAO:Cr^{3+},Nd^{3+} can achieve high NIR output powers of 46.37 and 42.82 mW at 100 mA and photoconversion efficiencies of 20.27 and 18.84% at a driving current of 20 mA, respectively. Furthermore, the NIR pc-LED package demonstrated excellent capability for penetrating biological tissues, effectively distinguishing between pork, chicken, and beef. These results suggest that the phosphors can be utilized for non-destructive monitoring applications.

1. Introduction

NIR luminescent materials have extensive applications across fields such as night vision, remote control, bio-imaging, food composition analysis, iris recognition, optical communication, targeted therapy, and tumor diagnosis due to their emission spectra spanning various NIR intervals. The emergence of high-power broadband NIR light sources based on laser-excited phosphors can enable the above-mentioned wide range of applications compared to conventional tungsten halogen and incandescent lamps.[1–3] Specifically, non-destructive detection of organic compounds can be accomplished by analyzing the distinct spectral features of C–H, O–H, and N–H bonds within the short-wave NIR range (700–1100 nm). This spectral range is enabled by NIR phosphor-converted light-emitting diodes (pc-LEDs), which offer environmentally friendly, cost-effective, long-lasting, and highly stable solutions, making them ideal NIR light sources for numerous practical applications. The essential component of these devices is the phosphor, and selecting a suitable phosphor is crucial for advancing NIR pc-LED technology.[4–6]

In recent years, various near-infrared phosphors doped with different ions have been developed. Eu^{2+} has an f–d electronic configuration and exhibits broad emission properties, and Zhiguo Xia's team reported a novel Eu^{2+}-activated broadband NIR-emitting phosphor $BaSrGa_4O_8:Eu^{2+}$ with a tunable emission spectrum achieved by adjusting the Ba/Sr atomic ratio.[7] However, its emission peaks usually fall in the deep red region, leading to insufficient emission in the longer wavelength range. In contrast, Cr^{3+} ion-doped luminescent materials have attracted much attention from researchers due to their tunable emission in the near-infrared region. Cr^{3+} ions possess a distinct structure typical of transition metal ions, in which the outermost electron layer lacks full electron occupancy, making them sensitive to the influence of the local structure. Within the crystal field environment of an intermediate state, characterized by Dq/B values close to 2.3, the energy levels of ^2E and $^4T_2$ intersect, resulting in orbital mixing.[8,9] This intermediate crystal field environment induces both strong and weak crystal fields in the Cr^{3+} activated system, manifesting sharp narrowband and broadband emissions in the photoluminescence (PL) spectrum. The garnet crystal structure, known for its dense nature, stands out as an exceptional host for Cr^{3+} doping compared with other matrices. This garnet system exhibits remarkable luminescence efficiency and thermal stability, making it a preferred

[a]*College of Rare Earths, Jiangxi University of Science and Technology, Ganzhou, Jiangxi 341000, P. R. China. E-mail: xinyye@yahoo.com*
[b]*Key Laboratory of Rare Earths and Institute of Material and Chemistry, Ganjiang Innovation Academy, Chinese Academy of Sciences, Ganzhou 341000, P. R. China. E-mail: hpyou@ciac.ac.cn*
† Electronic supplementary information (ESI) available. See DOI: https://doi.org/10.1039/d4qi02260b

choice for constructing broadband near-infrared (NIR) phosphors.[10] In the garnet structure ($A_3B_2C_3O_{12}$), the B^{3+} site offers a hexagonal octahedral crystal field environment. Substituting B^{3+} with Cr^{3+} typically yields near-infrared luminescence within the 650–950 nm range. However, there is often a necessity to develop luminous materials that emit at longer wavelengths beyond 980 nm.

Materials emitting within the first (650–900 nm) and second (1000–1350 nm) biological windows garner significant attention due to their broad applications in biological imaging and instrumentation.[11] Ln^{3+} ions, notably Yb^{3+} and Nd^{3+}, exhibit longer-wavelength near-infrared emission capabilities.[12] Yb^{3+} ions, with a single excited state energy level at $^2F_{5/2}$, emit near-infrared light around 1000 nm, while Nd^{3+} ions offer absorption spanning from UV to NIR, emitting at 1060 nm ($^4F_{3/2} \rightarrow {}^4I_{11/2}$), meeting the requirements for *in vitro* optical imaging.[13] However, the limitations of NIR luminescent materials stem from narrow emission bandwidths and excitation peak mismatches with blue chips. Addressing this challenge involves leveraging energy transfer between Cr^{3+} and Ln^{3+} ions. Codoping Cr^{3+} and Ln^{3+} ions enables continuous emission bands in longer wavelength ranges, thereby enhancing the NIR emission efficiency. Recent research has utilized Cr^{3+} to sensitize Yb^{3+} or Nd^{3+} ions, achieving NIR emissions within the 650–1100 nm range. He *et al.* reported Cr^{3+} and Yb^{3+} codoped $Ca_2LuZr_2Al_3O_{12}$ broadband near-infrared phosphors by the energy transfer from Cr^{3+} to Yb^{3+} ions, and Yb^{3+} doping improved its thermal stability.[14] Wang *et al.* reported the energy transfer *via* the Cr^{3+} to Nd^{3+} ions in $Ca_3In_2Ge_3O_{12}$:0.07Cr^{3+},0.15Nd^{3+}.[15] These results reveal that the garnet structure matrix codoped with Cr^{3+} and Yb^{3+}/Nd^{3+} is an ideal choice for investigating NIR luminescent phosphors with excellent thermal stability.

In this study, we report a YSAO:Cr^{3+} near-infrared phosphor with high luminescence efficiency (IQE/EQE = 88.4%/39.17%) and good thermal stability (89.7%/150 °C). The introduction of Yb^{3+}/Nd^{3+} into YSAO:Cr^{3+} forms YSAO:Cr^{3+},Yb^{3+}/YSAO:Cr^{3+}, Nd^{3+}, achieving an efficient energy transfer from the Cr^{3+} to Yb^{3+}/Nd^{3+} ions, respectively. YSAO:Cr^{3+},Yb^{3+} and YSAO:Cr^{3+}, Nd^{3+} have excellent thermal stability. The energy transfer from the Cr^{3+} to Yb^{3+}/Nd^{3+} ions was analyzed by studying the luminescence properties of the material. Near-infrared pc-LEDs were obtained by encapsulating phosphors with 450 nm blue LED chips, demonstrating possible applications in non-destructive analysis and night vision.

2. Experimental

2.1. Sample synthesis

A series of YSAO:$x$$Cr^{3+}$, YSAO:0.10$Cr^{3+}$,$y$$Yb^{3+}$ and YSAO:0.10Cr^{3+},$y$$Nd^{3+}$ was synthesized by high temperature solid-state reactions. The starting materials include Y_2O_3 (99.999%), Sc_2O_3 (99.99%), Al_2O_3 (99.99%), Cr_2O_3 (99.99%), Yb_2O_3 (99.99%), Nd_2O_3 (99.99%) and H_3BO_3 (A.R.). H_3BO_3 was used as a flux with a doping amount of 2% of the total mass. After weighing the ingredients according to stoichiometric proportions, the mixtures were ground for 20 minutes in an agate mortar. The resulting mixtures were transferred to alumina crucibles and sintered at 1773 K for 4 hours under nitrogen. Finally, the samples were reground for further characterization.

2.2 Characterization

X-ray diffraction (XRD) analysis of the powder samples was performed using an AXS D8 Advance instrument from Bruker (Germany) with CuKα radiation (λ = 0.15405 nm). The instrument's measurement range was set between 10° and 80° with a step size of 0.02° and a dwell time of 1 second per step. The voltage and current were maintained at 40 kV and 40 mA. X-ray photoelectron spectroscopy (XPS) was conducted using an AXIS SUPRA+ model spectrometer from Shimadzu to analyze the surface elements and chemical states of the materials. High-resolution field emission scanning electron microscopy (HRFE-SEM) (model JSM-IT800, JEOL, Japan) was used to obtain energy-dispersive X-ray spectroscopy (EDS) data for investigating the microstructure and morphology of the samples. Photoluminescence excitation (PLE) and photoluminescence (PL) spectra were recorded using an FLS1000 fluorescence spectrometer from Edinburgh Instruments, which is outfitted with a continuous xenon lamp and visible/NIR photomultiplier tube (PMT) detectors (Hamamatsu P9289P and R5509), with which the thermal stability of the samples and fluorescence lifetimes were also assessed. Quantum efficiency (QE) was determined using an integrating sphere combined with a spectrometer. The optoelectronic performance of the NIR pc-LEDs was assessed and analyzed with the aid of an integrating sphere spectral radiometer system (HASS-2000, 350–1650 nm, Everfine).

2.3 NIR pc-LED device fabrication

To fabricate a NIR pc-LED, YSAO:Cr^{3+},Yb^{3+} and YSAO:Cr^{3+},Nd^{3+} phosphors were thoroughly mixed with silicone resins A and B in a 1 : 1 ratio. The resulting mixture was then applied to the top surface of a 450 nm blue InGaN chip. The final optical device was cured at 100 °C for 1 hour. The fabricated near-infrared pc-LED was driven under currents ranging from 20 to 150 mA.

3. Results and discussion

As shown in Fig. 1a, the space group of YSAO is $Ia\bar{3}d$ (230). The crystal structure of YSAO contains three types of polyhedra: the [AlO_4] tetrahedron, the [(Al/Sc)O_6] octahedron, and the [YO_8] dodecahedron. The [YO_8] dodecahedra combine to form triangular units through edge-sharing, with these triangular units interfacing with one face of the [(Al/Sc)O_6]octahedra. The corresponding faces of the [(Al/Sc)O_6] octahedra is in contact with other triangular units of the dodecahedra. The [AlO_4] tetrahedra connect to the dodecahedra through edge-sharing in a rotational manner, thereby establishing a complex three-

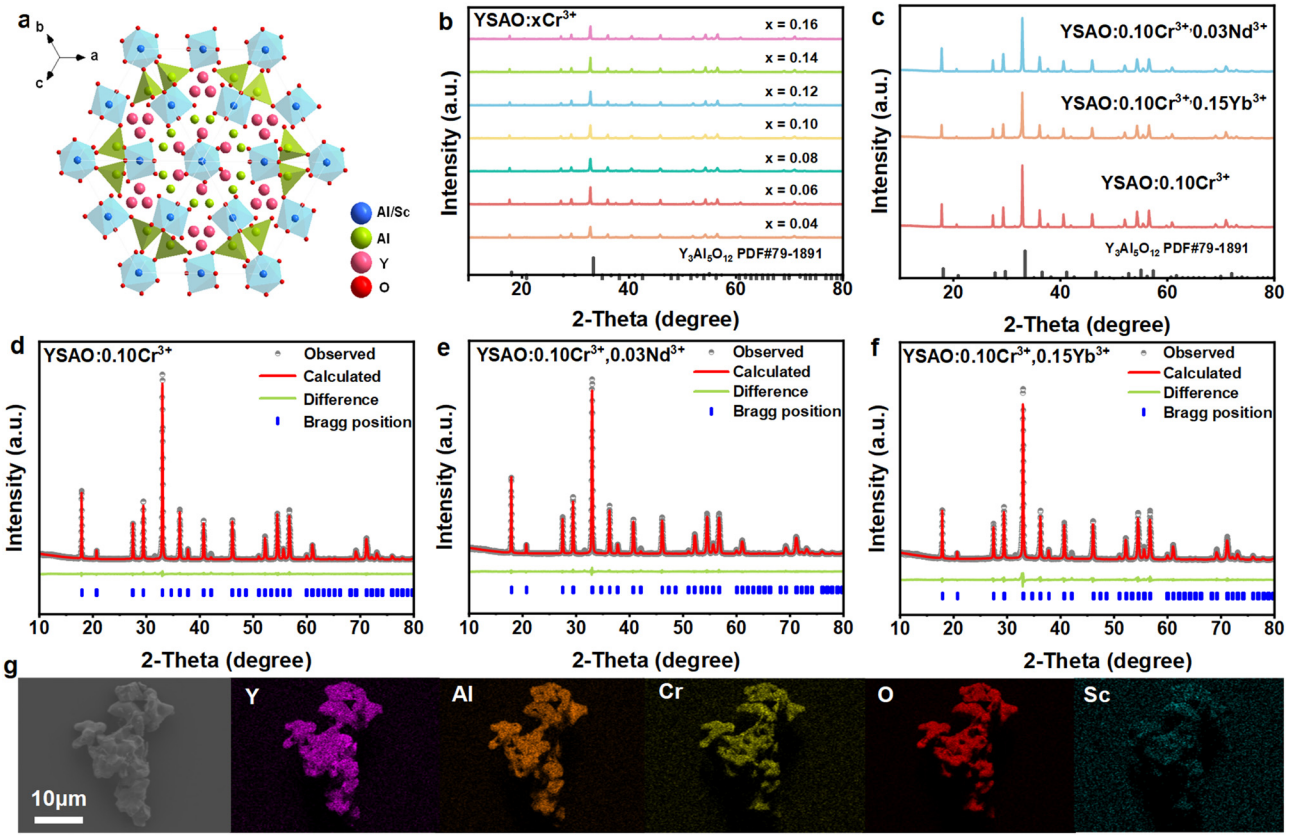

Fig. 1 (a) Crystal structure of the YSAO phase; (b) XRD patterns of YSAO:xCr^{3+} ($0.04 \leq x \leq 0.16$); (c) XRD patterns of YSAO:0.10Cr^{3+}, YSAO:0.10Cr^{3+},0.15Yb^{3+} and YSAO:0.10Cr^{3+},0.03Nd^{3+}; Rietveld refinements of (d) YSAO:0.10Cr^{3+}, (e) YSAO:0.10Cr^{3+},0.03Nd^{3+}, and (f) YSAO:0.10Cr^{3+},0.15Yb^{3+}; (g) SEM map of YSAO:0.10Cr^{3+} and EDS elemental distribution.

dimensional network.[16] Considering the ionic radius and valence, Cr^{3+} ions replace the Sc^{3+}/Al^{3+} sites and the Y^{3+} sites are suitable for Nd^{3+} and Yb^{3+} ions. Fig. 1b and c depict the XRD patterns of YSAO:xCr^{3+} ($0.04 \leq x \leq 0.16$), YSAO:0.10Cr^{3+},0.15Yb^{3+} and YSAO:0.10Cr^{3+},0.03Nd^{3+}, respectively. The diffraction peaks are in excellent correspondence with the standard pattern of $Y_3Al_5O_{12}$ (JCPDS 01-079-1891), suggesting the formation of a pure phase. The lattice expansion caused by the substitution of Sc^{3+} (CN = 6, r = 0.745 Å) for Al^{3+} (CN = 8, r = 0.535 Å) results in a shift of the position of the diffraction peaks to smaller angles. To further confirm the phase purity of the samples, YSAO:0.10Cr^{3+}, YSAO:0.10Cr^{3+},0.15Yb^{3+} and YSAO:0.10Cr^{3+},0.03Nd^{3+} samples were refined as shown in Fig. 1d, e and f. The fitting parameters for the samples YSAO:0.10Cr^{3+}, YSAO:0.10Cr^{3+},0.15Yb^{3+}, and YSAO:0.10Cr^{3+},0.03Nd^{3+} are R_{wp} = 7.05%, R_p = 4.725%; R_{wp} = 6.47%, R_p = 4.29%; and R_{wp} = 7.58%, R_p = 5.62%, respectively. All refinement reliability parameters are below 10%, indicating that the samples possess good phase purity. These results reveal that Cr^{3+}, Yb^{3+}, and Nd^{3+} ions were successfully doped into the YSAO matrix without forming any impurity phases. The corresponding results of the refinement are presented in Table S1.† A representative YSAO:0.10Cr^{3+} sample was analyzed by SEM to investigate its morphological characteristics, as illustrated in Fig. S2.† Its microstructure consists of irregular fragments of varying sizes between 2 and 5 μm. The EDS elemental maps in Fig. 1g show that elements such as Y, Sc, Al, O and Cr are evenly distributed in the phosphor particles.

The high-resolution spectra corresponding to the deconvoluted peaks of Y-3d, Al-2p, Sc-2p, C-1s, O-1s, and Cr-2p elements are shown in Fig. S3.† The elements Y, Sc, Al, O, and Cr were observed in the XPS spectrum of YSAO:0.10Cr^{3+} (in Fig. 2a and Fig. S4†). The peaks at 576.8 and 586.5 eV are ascribed to the $2p_{3/2}$ and $2p_{1/2}$ electrons of Cr^{3+}, respectively, which are consistent with the reported binding energies of Cr^{3+} ions at octahedral sites.[17] The PLE and PL spectra of YSAO:0.10Cr^{3+} are depicted in Fig. 2b. The two broad excitation bands are located at about 440 and 603 nm, corresponding to the $^4A_2 \rightarrow {}^4T_1(4F)$ and $^4A_2 \rightarrow {}^4T_2(4F)$ transitions of the Cr^{3+} ions, respectively. The emission spectrum contains narrowband emission from the $^2E \rightarrow {}^4A_2$ (689 nm) transition and broadband emission from the $^4T_2 \rightarrow {}^4A_2$ transition. The PL spectra and intensities of YSAO:xCr^{3+} ($0.04 \leq x \leq 0.16$) at various Cr^{3+}-concentrations are presented in Fig. S5† and Fig. 2c, respectively. The optimized Cr^{3+} doping concentration is 0.10, beyond which concentration quenching occurs. Through calculation and analysis, the dipole–dipole effect

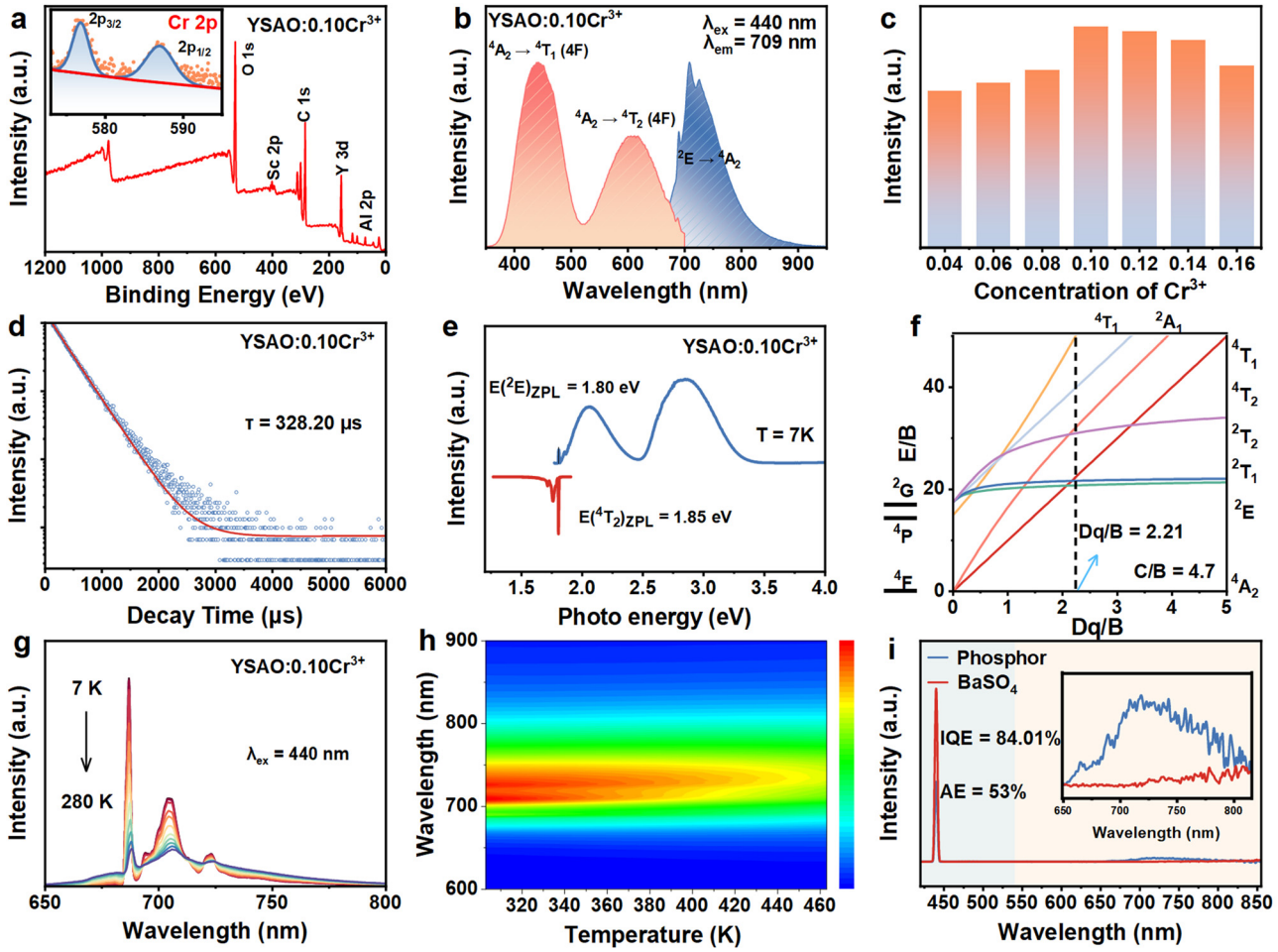

Fig. 2 (a) Typical XPS survey spectra of YSAO:0.10Cr^{3+} and illustration of high-resolution Cr-2p; (b) PLE and PL spectra of YSAO:0.10Cr^{3+} at room temperature; (c) emission intensity of YSAO:xCr^{3+} (x = 0.04–0.16); (d) single-exponential fitting decay curve of YSAO:0.10Cr^{3+}; (e) PL and PLE spectra of YSAO:0.10Cr^{3+} at T = 7 K; (f) Tanabe–Sugano energy level diagram of Cr^{3+} in YSAO; (g) temperature dependent PL spectra of YSAO:0.10Cr^{3+} upon 440 nm excitation (T = 7–280 K); (h) contour plot of the emission spectra (λ_{ex} = 440 nm) of YSAO:0.10Cr^{3+} recorded within the temperature range of 303–483 K; (i) IQE and AE measurement of YSAO:0.10Cr^{3+}.

dominates concentration quenching (ESI Note S1 and Fig. S6†). Fig. 2d illustrates the decay curve of YSAO:0.10Cr^{3+} excited at 440 nm and monitored at 710 nm, which can be well fitted by single-exponential functions:[18]

$$I(t) = I_0 + A\exp\left(-\frac{t}{\tau}\right) \quad (1)$$

where I_0 and $I(t)$ denote the initial emission intensity and the emission intensity at time t, respectively. A denotes the fitting constant, while t and τ indicate the time and lifetime, respectively. The fluorescence lifetime was found to be 328.20 μs by fitting. As the concentration of Cr^{3+} increases, the lifetime gradually decreases from 357.54 to 289.73 μs (in Fig. S7†), which is mainly caused by the non-radiative transition.

In general, the crystal field strength can be assessed by calculating the crystal field splitting energy (Dq) and the Racah parameter (B) obtained from the emission and excitation spectra, as follows:[19,20]

$$Dq = \frac{1}{10}E(^4A_2 \rightarrow {}^4T_2) = \frac{1}{10}(^4T_2)_{ZPL} \quad (2)$$

$$B = 6.18Dq - \frac{1}{2}\left[(12.36Dq)^2 - 2.22E(^2E)_{ZPL}Dq\right]^{\frac{1}{2}} \quad (3)$$

$$E(^4T_1)_{ZPL} = 7.5B + 15Dq - \frac{Dq}{2}\left[\left(\frac{15B}{Dq} + 10\right)^2 - \frac{480B}{Dq}\right]^{\frac{1}{2}} \quad (4)$$

where B is the Racah parameter and Dq is the crystal field intensity. The precise energy position of $E(^2E)_{ZPL}$ can be identified using the spike at 1.8 eV in the PLE spectrum at 7 K, as illustrated in Fig. 2e. On the basis of the previous work of Adachi, we suggest that $E(^4T_2)_{ZPL}$ is about 1.85 eV, which is close to the onset of the PLE spectrum shown in Fig. 2e. As shown in Fig. 2f, the

values of Dq/B and $E(^4T_1)_{ZPL}$ are calculated to be 2.21 and 2.66 eV according to eqn (2)–(4), indicating that the chromium ions are in the intermediate crystal field of the YASO matrix. In this case, the $^4T_2 \rightarrow {}^4A_2$ spin-permissive transition and the $^2E \rightarrow {}^4A_2$ spin-permissive transition can occur concurrently. This corresponds to the observation that the emission spectra exhibit both narrow-band and broadband emission.[21]

The low-temperature spectra demonstrate that the spectrum of YSAO:0.10Cr^{3+} consists solely of the narrow-band $^2E \rightarrow {}^4A_2$ transitions, accompanied by the N lines and the corresponding phonon sidebands (in Fig. 2g). Fig. 2e shows that the R line produced by the $^2E \rightarrow {}^4A_2$ transitions splits into two: R1 (14 584.70 cm^{-1}) and R2 (14 559.22 cm^{-1}), with a difference of 25.48 cm^{-1} in wavenumber. The R-line splitting results from the influence of the non-cubic crystal field and spin–orbit coupling, which leads to the splitting of the ^2E energy levels.[22] With increasing temperature, the emission intensity of the R and N lines decreases rapidly relative to the broadband, and the emission band of YSAO:0.10Cr^{3+} gradually broadens. In an intermediate crystal field environment of six-coordinated octahedra, Cr^{3+} ions exhibit $^2E \rightarrow {}^4A_2$ spike emission at low temperatures (*e.g.*, 7 K), whereas the $^4T_2 \rightarrow {}^4A_2$ gradually dominates as the temperature increases. Since the ^2E energy level is situated below the $^4T_2$ energy level, the latter can be thermally occupied at higher temperatures. According to the spin-selection rule, the probability of the $^4T_2 \rightarrow {}^4A_2$ transition is higher than that of the $^2E \rightarrow {}^4A_2$ transition. Consequently, the broadband emission from the $^4T_2 \rightarrow {}^4A_2$ transition can rapidly dominate the PL spectrum. Under 440 nm excitation, the emission spectra of YSAO:0.10Cr^{3+} were obtained at various temperatures ranging from 303 to 483 K, as illustrated in Fig. 2h. At 423 K, the emission intensity is 89.7% of that at room temperature, suggesting that YSAO:Cr^{3+} shows excellent thermal stability. By calculation, the activation energy is found to be 0.25 eV (ESI Note S2 and Fig. S8†). The YSAO:0.10Cr^{3+} phosphor endows an internal quantum efficiency of 84.01% under 440 nm blue light excitation, as depicted in Fig. 2i (ESI Note S3†). These values suggest that the YSAO:0.10Cr^{3+} phosphor possesses exceptional photoluminescence properties, which are advantageous for the development of NIR luminescence applications, particularly in high-performance PC-LEDs.[16]

The energy transfer from the Cr^{3+} to Nd^{3+}/Yb^{3+} ions was established by introducing Nd^{3+}/Yb^{3+} into YSAO:0.10Cr^{3+}. Fig. 3a presents the PLE spectra monitored at emission wavelengths of the Yb^{3+} (1030 nm) and Nd^{3+} (1062 nm) ions, respectively. They consist of the main excitation bands of the $^4A_2 \rightarrow {}^4T_1$ and $^4A_2 \rightarrow {}^4T_2$ transitions of the Cr^{3+} ions, indicating that the main excitation energy comes from the absorption of the Cr^{3+} ions. Under excitation at 440 nm, the PL spectra of YSA0:Cr^{3+},Nd^{3+} and YSA0:Cr^{3+},Yb^{3+} show the characteristic peaks of Cr^{3+}, Yb^{3+}, and Nb^{3+} ions (Fig. 3b). The emission peaks in the range of 900–1050 nm originate from the $^2F_{5/2} \rightarrow {}^2F_{7/2}$ transitions of the Yb^{3+} ions in YSAO:Cr^{3+},Yb^{3+}, while the emission bands in the range of 850–1100 nm of YSAO:Cr^{3+}, Nd^{3+} correspond to the $^4F_{3/2} \rightarrow {}^4I_{9/2}$ and $^4F_{3/2} \rightarrow {}^4I_{11/2}$ transitions of the Nd^{3+} ions, respectively.[23] These results indicate that Cr^{3+} ions can effectively transfer energy to the Yb^{3+} and Nd^{3+} ions. The thermal stability of phosphors is an essential index for assessing the high-temperature luminescence properties. To further investigate the effect of Yb^{3+} and Nd^{3+} on the thermal stability of the YSAO:0.10Cr^{3+} phosphor, the temperature-dependent PL spectra of YSAO:0.10Cr^{3+},0.03Nd^{3+} and YSAO:0.10Cr^{3+},0.15Yb^{3+} phosphors under 440 nm excitation were recorded, as shown in Fig. 3c and e. At a temperature of 423 K, the luminous intensity of YSAO:0.10Cr^{3+},0.03Nd^{3+} and YSAO:0.10Cr^{3+},0.15Yb^{3+} can still be maintained at 99.73% and 94.65% at room temperature, respectively (Fig. 3d and f). As the temperature increases, the rise in non-radiative transitions results in a decrease in the PL intensity of Cr^{3+} ions (89.7% at 423 K). However, the introduction of Nd^{3+} ions enhances the energy transfer efficiency between Cr^{3+} and Nd^{3+} ions with increasing temperature, enabling Cr^{3+} ions to transfer more absorbed energy to Nd^{3+} ions. This further reduces thermal quenching, with the characteristic emission of Nd^{3+} ions, exhibiting excellent thermal stability. Consequently, this enhances the overall thermal stability of the sample. Yb^{3+} possesses a straightforward ground state ($^2F_{7/2}$) and an excited state ($^2F_{5/2}$), minimizing energy loss due to cross-relaxation between distinct energy levels. A competitive relationship exists between the thermal quenching of the Cr^{3+}-emission and the energy transfer from the Cr^{3+} to Yb^{3+} ions.[24–26] Therefore, the introduction of Nd^{3+} and Yb^{3+} controls the energy transfer pathway from the luminescence quenching center (Cr^{3+}) to the thermally stable centers ($Nd^{3+}$and Yb^{3+}), inhibiting the non-radiative energy dissipation of Cr^{3+} and enhancing the thermal stability of luminescence.

Fig. 4a and d show the PL spectra (λ_{ex} = 440 nm) of YSAO:0.10Cr^{3+},$y$$Nd^{3+}$ (y = 0.01–0.18) and YASO:0.10Cr^{3+},$y$$Yb^{3+}$ (y = 0.03–0.60), respectively. It is evident that the emission intensity of the Nd^{3+}/Yb^{3+} ions reaches a maximum at y = 0.03 or y = 0.15, while the emission intensity of the Cr^{3+} ions decreases monotonically. These phenomena further indicate the energy transfer from the Cr^{3+} to Nd^{3+}/Yb^{3+} ions in YSAO:0.10Cr^{3+},Nd^{3+} and YASO:0.10Cr^{3+},Yb^{3+}. Fig. 4b and e present the decay curves of YSAO:0.10Cr^{3+},$y$$Nd^{3+}$ and YSAO:0.10Cr^{3+},$y$$Yb^{3+}$ under 440 nm excitation and 707 nm monitoring. The fluorescence lifetimes of the Cr^{3+} ions at varying y values are determined as follows:[27,28]

$$\tau = \frac{\int_0^\infty tI(t)\mathrm{d}t}{\int_0^\infty I(t)\mathrm{d}t} \quad (5)$$

As the concentration of Nd^{3+}/Yb^{3+} increases, the photoluminescence lifetimes of the Cr^{3+} ions decrease from 252.38 to 19.02 μs or 234.11 to 13.22 μs, respectively. The shortened lifetime further demonstrates the energy transfer from the Cr^{3+} to Yb^{3+}/Nd^{3+} ions. The energy transfer efficiency was calculated using the following expression:[29]

$$\eta_{ET} = 1 - \frac{\tau}{\tau_0} \quad (6)$$

Here, τ and τ_0 represent the corresponding decay times of the Cr^{3+} ions in the presence and absence of Yb^{3+}/Nd^{3+} ions,

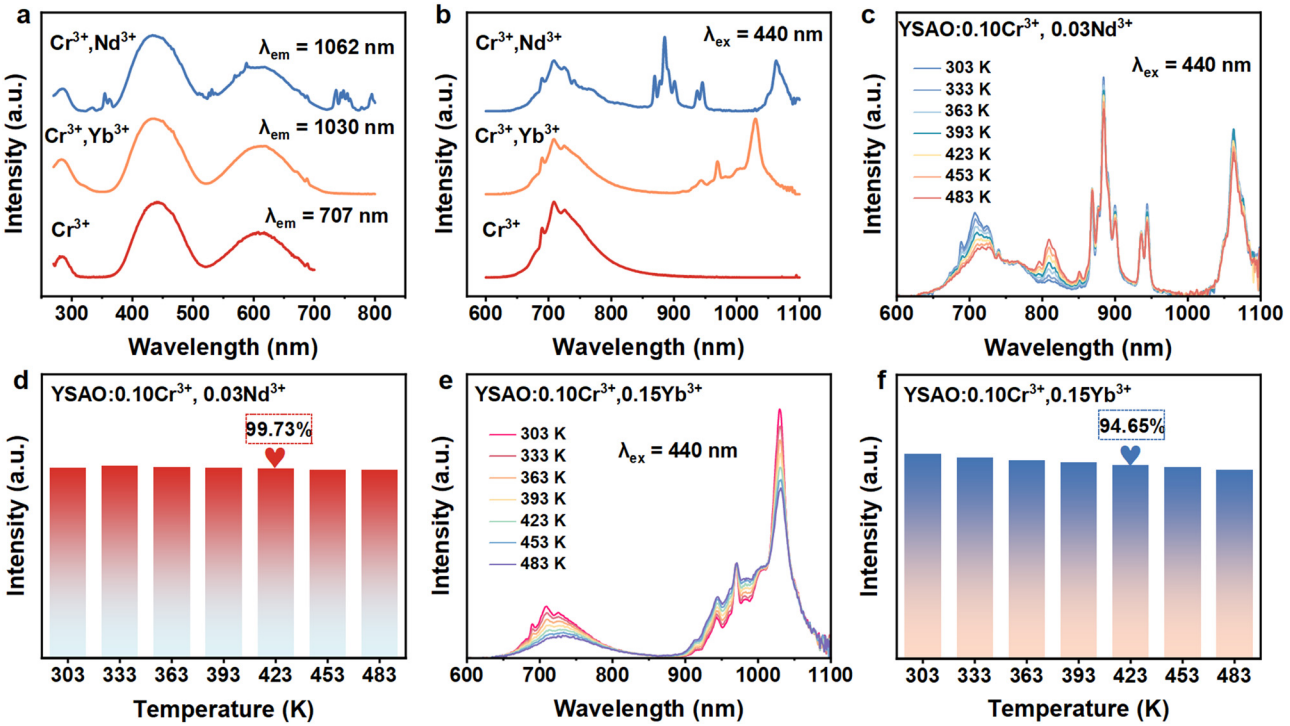

Fig. 3 (a) PLE spectra of YSAO:0.10Cr^{3+}, YSAO:Cr^{3+},Yb^{3+} and YSAO:Cr^{3+},Nd^{3+}; (b) PL spectra of YSAO:0.10Cr^{3+}, YSAO:Cr^{3+},Yb^{3+} and YSAO:Cr^{3+},Nd^{3+} under 440 nm excitation; (c) PL spectra of the YSAO:0.10Cr^{3+},0.03Nd^{3+} phosphor at different temperatures; (d) emission intensity of YSAO:0.10Cr^{3+},0.03Nd^{3+} (T = 303–483 K); (e) PL spectra of the YSAO:0.10Cr^{3+},0.15Yb^{3+} phosphor at different temperatures; (f) emission intensity of YSAO:0.10Cr^{3+},0.15Yb^{3+} (T = 303–483 K).

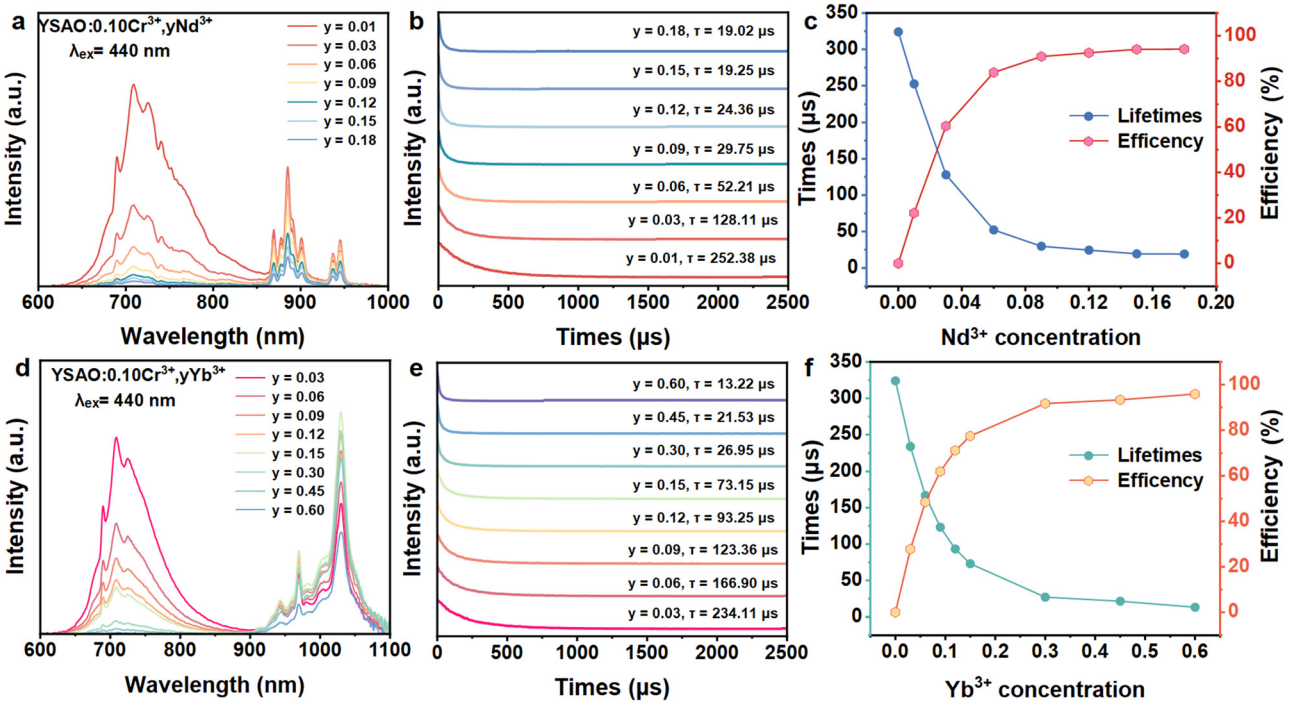

Fig. 4 (a) Concentration-dependent PL spectra of YSAO:0.10Cr^{3+},$y$$Nd^{3+}$ (y = 0.01–0.18); (b) PL decay curves of YSAO:0.10Cr^{3+},$y$$Nd^{3+}$ (y = 0.01–0.18) at 707 nm; (c) energy transfer efficiency in YSAO:0.10Cr^{3+},$y$$Nd^{3+}$ (y = 0.01–0.18); (d) concentration-dependent PL spectra of YSAO:0.10Cr^{3+},$y$$Yb^{3+}$ (y = 0.03–0.60); (e) PL decay curves of YASO:0.10Cr^{3+},$y$$Yb^{3+}$ (y = 0.03–0.60) at 707 nm; (f) energy transfer efficiency in YSAO:0.10Cr^{3+},$y$$Yb^{3+}$ (y = 0.03–0.60).

respectively. Fig. 4c and f show the luminescence lifetimes and energy transfer efficiencies. The maximum transfer efficiencies from the Cr^{3+} to Nd^{3+}/Yb^{3+} ions are 94.13/95.92%. These results suggest that the energy transfer from the Cr^{3+} to Nd^{3+}/Yb^{3+} ions is highly efficient. Typically, energy transfer between the sensitizer and the activator may occur through resonance interactions, which encompasses exchange interactions and multipolar interactions. On the basis of the refinement results, the unit cell volumes (V) of YSAO:Cr^{3+},Yb^{3+} and YSAO:Cr^{3+}, Nd^{3+} are 1792.55 Å^3 and 1793.034 Å^3, respectively. Here, N is 16, and x_c represents the sum of the concentrations of Cr^{3+} and Yb^{3+} ions, and Cr^{3+} and Nd^{3+} ions, at which the emission intensity of Cr^{3+} ions is reduced by half. Through calculations, we obtained R_c values of 11.81 and 11.02 Å, respectively, both of which are significantly greater than 5 Å. Therefore, we can infer that the energy transfer mechanism from the Cr^{3+} to Nd^{3+}/Yb^{3+} ions in YSAO is primarily due to multipolar interactions. According to the approximation of Reisfeld and the theory of multipolar interaction of Dexter, the nature of the multipolar interaction between donor and acceptor ions can be determined using the following equation:[15,30]

$$\frac{I_0}{I} \propto C^{\frac{\theta}{3}} \quad (7)$$

I_0 denotes the integral intensity of the Cr^{3+} ion emission in YSAO without Yb^{3+}/Nd^{3+} doping. I is the integral intensity of the Cr^{3+} ions in the presence of the Nd^{3+}/Yb^{3+} ions, and C signifies the combined concentration of the Cr^{3+} and Nd^{3+}/Yb^{3+} ions. The relationships between I_0/I and $C^{\theta/3}$ are given in Fig. S9.† The data of YSAO:0.10Cr^{3+},$y$$Nd^{3+}$ and YSAO:0.10Cr^{3+}, $y$$Yb^{3+}$ samples all fit best at θ = 10, corresponding to the quadrupole–quadrupole interaction. Fig. S10† presents the energy transfer model for YSAO:Cr^{3+},Yb^{3+}/Nd^{3+}. Upon excitation at 450 nm, the electrons in the Cr^{3+} ions transition from the ground state $^4A_2$ to an excited state and then relax to the lowest excited state $^4T_2$. Subsequently, a portion of these electrons return to the ground state $^4A_2$, emitting near-infrared radiation that covers the 650–900 nm range. Some of the energy is transferred to Yb^{3+} ions, causing electrons to be excited from the $^2F_{7/2}$ state to the $^2F_{5/2}$ state, and finally returning to the $^2F_{7/2}$ state, resulting in emission around 1000 nm in the long wavelength region.[31] As for the case of the Cr^{3+} and Nd^{3+} ions, the energy is transferred to the $^4F_{5/2}$ or $^4F_{7/2}$ levels of Nd^{3+}. Subsequently, electrons are released to the $^4F_{3/2}$ level, thereby enhancing the emission bands at 885 nm (11 441 cm^{-1}, $^4F_{3/2} \rightarrow {}^4I_{9/2}$) and 1062 nm (9697 cm^{-1}, $^4F_{3/2} \rightarrow {}^4I_{11/2}$).[32]

In order to evaluate the practical application potential of YSAO:Cr^{3+},Yb^{3+} and YSAO:Cr^{3+},Nd^{3+} phosphors, we coated these phosphors on a 450 nm blue chip to obtain NIR pc-LEDs. As shown in Fig. 5a and c, the emission intensity gradually increases as the drive current increases from 20 to 150 mA. Fig. 5b and d illustrate that the NIR emission output power also increases with increasing current, while the NIR photoelectric conversion efficiency gradually decreases. At a driving

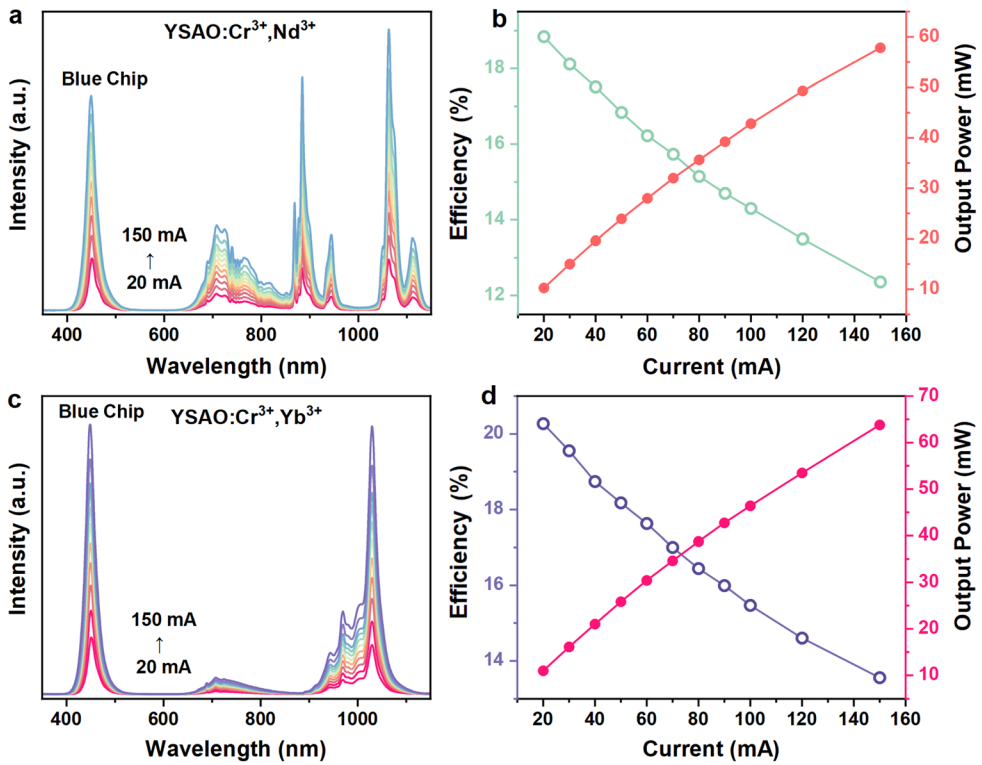

Fig. 5 (a) PL spectra of YSAO:Cr^{3+},Nd^{3+} pc-LEDs at different drive currents; (b) the output power and photoelectric conversion efficiency; (c) PL spectra of YSAO:Cr^{3+},Yb^{3+} pc-LEDs at different drive currents; (d) the output power and photoelectric conversion efficiency.

current of 100 mA, the near-infrared output powers of YSAO:Cr^{3+},Yb^{3+} and YSAO:Cr^{3+},Nd^{3+} reach 46.37 and 42.82 mW, respectively, and NIR photoelectric conversion efficiencies are 15.47 and 14.30%, respectively. Relative to the previously reported NIR emission phosphors (in Table 1), the prepared YSAO:Cr^{3+},Yb^{3+} and YSAO:Cr^{3+},Nd^{3+} have excellent performances, demonstrating their potential for versatile applications.

The absorption spectrum of food in the near-infrared region primarily arises from the overtones and combination bands of hydrogen-containing groups, such as –CH, –NH, and –OH. These absorption bands are predominantly distributed within the range of 700 to 1500 nm.[39,40] The absorption of near-infrared light varies due to the different types and amounts of hydrogen-containing groups. Consequently, the

Table 1 Optoelectronic performance of Cr^{3+}/Ln^{3+} doped long-wave broadband near-infrared phosphors for pc-LED devices

Phosphors	Current	Output power	Electro-optical conversion efficiencies	Ref.
YSAO:0.10Cr^{3+},0.06Nd^{3+}	100 mA	42.82 mW	14.30%	This work
YSAO:0.10Cr^{3+},0.15Yb^{3+}	100 mA	46.37 mW	15.47%	This work
$Gd_3MgScGa_2SiO_{12}$:0.04Cr^{3+},0.007Yb^{3+}	100 mA	19.5 mW	7.52%	33
$LiScP_2O_7$:0.06Cr^{3+},0.03Yb^{3+}.	100 mA	~36 mW	12%	26
$Ca_2LaHf_2Al_3O_{12}$:0.01Cr^{3+},0.01Yb^{3+}	200 mA	33.24 mW	10%	34
$Ca_2LuZr_2Al_3O_{12}$:0.08Cr^{3+},0.01Yb^{3+}	100 mA	41.8 mW	14.3%	14
$Ca_2YHf_2Al_3O_{12}$:0.02Cr^{3+},0.03Yb^{3+}	100 mA	18 mW	6%	35
$Y_3Ga_5O_{12}$:Cr^{3+},Yb^{3+}	100 mA	43.2 mW	14.3	36
$Sr_3SiAl_{10}O_{20}$:0.02Cr^{3+},0.01Yb^{3+}	100 mA	32.29 mW	~10%	37
$Gd_2GaSb_{0.9}Ta_{0.1}O_7$:0.03$Cr^{3+}$,0.04$Yb^{3+}$	100 mA	~22 mW	~8.5%	38

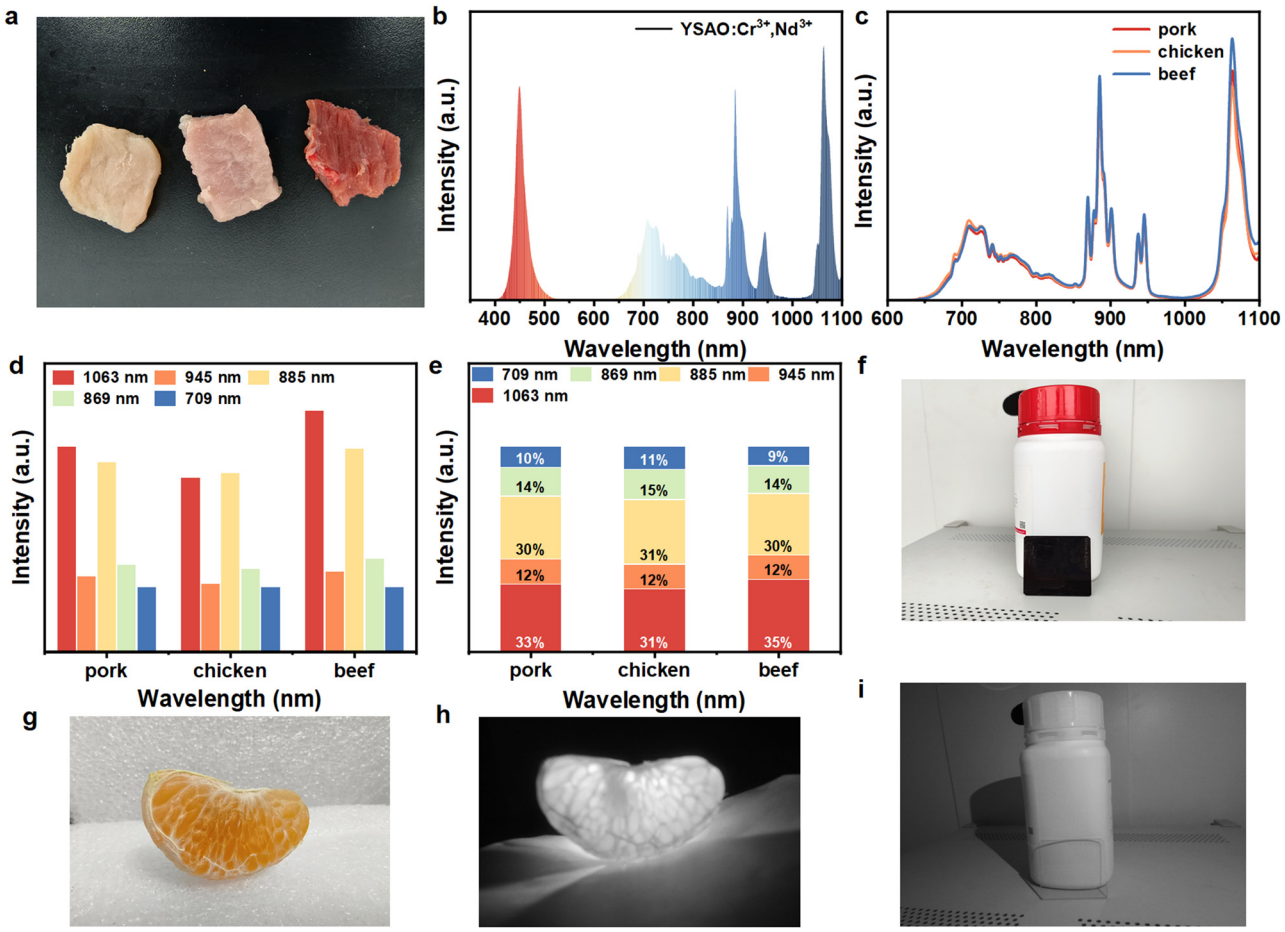

Fig. 6 (a) Spectrum of the NIR pc-LED; (b) spectrum after penetration of chicken, beef and pork; (c) display of chicken, beef and pork used in the experiment; (d) the intensity ratio between the emission peaks at 709 nm was normalized to 1; (e) percentage between normalized emission peak intensities; (f) visible and (i) near-infrared images of opaque plastic bottles illuminated by fluorescent lamps and manufactured near-infrared pc-LED lamps; and (g) visible and (h) near-infrared images of orange petals illuminated by fluorescent and fabricated near-infrared pc-LED lamps.

types of meat can be distinguished by the intensity ratio of different emission peaks. The experimental device used the YSAO:Cr^{3+},Nd^{3+} near-infrared phosphor. As shown in Fig. 6a, the thickness of chicken, beef and pork was 5 mm. After near-infrared light passes through the different meat components, the relative emission intensity changes significantly (Fig. 6b and c). Fig. 6d shows that the luminous intensity of chicken at 1060 nm is the lowest, while that of beef is the highest (using the luminous intensity at 710 nm as a reference). Additionally, the percentage of luminescence intensity of each meat component varies significantly in different areas (Fig. 6e). This makes meat analysis more convenient and intelligent. Therefore, multi-band NIR LEDs have potential applications in non-destructive testing analysis. Furthermore, we utilized the YSAO:Cr^{3+},Yb^{3+} NIR phosphor to validate the effectiveness of the NIR light source in night vision monitoring applications. As depicted in Fig. 6f, the portion of the object obscured by a 645 nm filter (an opaque plastic bottle) remains invisible under fluorescent lighting. However, when the fabricated NIR pc-LED device is activated in a dark environment, the NIR camera is able to clearly capture the objects, including those concealed by the 645 nm filter (as shown in Fig. 6i). Additionally, Fig. 6g and h exhibit photographs taken with an ordinary digital camera and a commercial short-wave infrared camera, respectively. Under indoor white light illumination, an ordinary digital camera cannot capture the internal structure of the orange. However, the pulp, seeds, and complex structure of the orange are clearly visible, when the near-infrared LED device is used for illumination.

4. Conclusion

In summary, a series of $Y_3ScAl_4O_{12}$ garnet NIR-emitting materials were synthesized, and codoping with Nd^{3+} and Yb^{3+} ions not only effectively broadened the NIR emission bandwidth of the materials but also improved their thermal stability, due to the efficient energy transfer among Cr^{3+} and Nd^{3+}/Yb^{3+} ions. These findings offer a pathway to enhance the thermal stability and energy transfer of Cr^{3+}-activated NIR emitters for use in NIR light-emitting diodes. Additionally, YSAO:Cr^{3+},Nd^{3+} and YSAO:Cr^{3+},Yb^{3+} phosphors were encapsulated with a blue LED chip to obtain NIR pc-LED devices, achieving maximum NIR light output powers of 42.82 and 46.37 mW, respectively, at a driving current of 100 mA. The results indicate that YSAO:Cr^{3+},Nd^{3+} and YSAO:Cr^{3+},Yb^{3+} phosphors have promising applications in the NIR spectrum, including potential uses in night vision imaging and non-destructive analysis techniques.

Data availability

The data that support the findings of this study are available in the ESI† of this article.

Conflicts of interest

The authors declare no conflict of interest.

Acknowledgements

This study was financially supported by the National Key Research and Development Program (grant no. 2022YFC2905201), the National Natural Science Foundation of China (grant no. 52072363 and 22305250), and the research fund of the Key Laboratory of Rare Earths, Chinese Academy of Sciences.

References

1 G. Liu, W. Chen, Z. Xiong, Y. Wang, S. Zhang and Z. Xia, Laser-driven broadband near-infrared light source with watt-level output, *Nat. Photonics*, 2024, **18**, 562–568.
2 Y. Shi, Z. Wang, J. Peng, Y. Wang, S. He, J. Li, R. Li, G. Wei, Y. Yang and P. Li, Achieving the ultra-broadband near-infrared $La_3SnGa_5O_{14}$:Cr^{3+} phosphor via multiple lattice sites occupation for biological nondestructive detection and night-vision technology, *Mater. Today Adv.*, 2022, **16**, 100305.
3 G. Liu, M. S. Molokeev, B. Lei and Z. Xia, Two-site Cr^{3+} occupation in the $MgTa_2O_6$:Cr^{3+} phosphor toward broadband near-infrared emission for vessel visualization, *J. Mater. Chem. C*, 2020, **8**, 9322–9328.
4 H. T. Zeng, T. L. Zhou, L. Wang and R. J. Xie, Two-Site Occupation for Exploring Ultra-Broadband Near-Infrared Phosphor-Double-Perovskite La_2MgZrO_6:Cr^{3+}, *Chem. Mater.*, 2019, **31**, 5245–5253.
5 Y. Wang, Z. Wang, G. Wei, Y. Yang, S. He, J. Li, Y. Shi, R. Li, J. Zhang and P. Li, Highly efficient and stable near–infrared broadband garnet phosphor for multifunctional phosphor–converted light–emitting diodes, *Adv. Opt. Mater.*, 2022, **10**, 2200415.
6 G. Liu, M. S. Molokeev and Z. Xia, Structural rigidity control toward Cr^{3+}-based broadband near-infrared luminescence with enhanced thermal stability, *Chem. Mater.*, 2022, **34**, 1376–1384.
7 Y. Zhu, X. Wang, J. Qiao, M. S. Molokeev, H. C. Swart, L. Ning and Z. Xia, Regulating Eu^{2+} multisite occupation through structural disorder toward broadband near-infrared emission, *Chem. Mater.*, 2023, **35**, 1432–1439.
8 A. Van Die, G. Blasse and W. Van Der Weg, Luminescence properties of Cr^{3+} doped borate glasses: Influence of crystal field strength and microcrystallite formation, *Mater. Chem. Phys.*, 1986, **14**, 513–523.
9 Z. Song, P. A. Tanner and Q. Liu, Host Dependency of Boundary between Strong and Weak Crystal Field Strength of Cr3+ Luminescence, *J. Phys. Chem. Lett.*, 2024, **15**, 2319–2324.

10 X. Yang, W. Chen, D. Wang, X. Chai, G. Xie, Z. Xia, M. S. Molokeev, Y. Liu and B. Lei, Near-infrared photoluminescence and phosphorescence properties of Cr^{3+}-doped garnet-type $Y_3Sc_2Ga_3O_{12}$, *J. Lumin.*, 2020, **225**, 117392.

11 D. Salo, H. R. Zhang, D. M. Kim and M. Y. Berezin, Multispectral measurement of contrast in tissue-mimicking phantoms in near-infrared spectral range of 650 to 1600 nm, *J. Biomed. Opt.*, 2014, **19**, 086008.

12 L. Kong, Y. Y. Liu, L. P. Dong, L. Zhang, L. Qiao, W. S. Wang and H. P. You, Near-infrared emission of $CaAl_6Ga_6O_{19}$:Cr^{3+}, Ln^{3+}(Ln = Yb, Nd, and Er) via energy transfer for c-Si solar cells, *Dalton Trans.*, 2020, **49**, 8791–8798.

13 Y. L. Wu, Y. Li, X. X. Qin, R. C. Chen, D. K. Wu, S. J. Liu and J. R. Qiu, Dual mode NIR long persistent phosphorescence and NIR-to-NIR Stokes luminescence in $La_3Ga_5GeO_{14}$:Cr^{3+}, Nd^{3+} phosphor, *J. Alloys Compd.*, 2015, **649**, 62–66.

14 S. He, L. L. Zhang, H. Wu, H. J. Wu, G. H. Pan, Z. D. Hao, X. Zhang, L. G. Zhang, H. Zhang and J. H. Zhang, Efficient Super Broadband NIR $Ca_2LuZr_2Al_3O_{12}$:Cr^{3+},Yb^{3+} Garnet Phosphor for pc-LED Light Source toward NIR Spectroscopy Applications, *Adv. Opt. Mater.*, 2020, **8**, 1901684.

15 T. Wang, L. W. Cao, Z. J. Wang and P. L. Li, Luminescence properties and energy transfer of the near-infrared phosphor $Ca_3In_2Ge_3O_{12}$:Cr^{3+}, Nd^{3+}, *RSC Adv.*, 2022, **12**, 28405–28413.

16 Z. Song, D. Zhou and Q. Liu, Tolerance factor and phase stability of the garnet structure, *Acta Crystallogr., Sect. C: Struct. Chem.*, 2019, **75**, 1353–1358.

17 L. You, R. D. Tian, T. L. Zhou and R. J. Xie, Broadband near-infrared phosphor $BaMgAl_{10}O_{17}$:Cr^{3+} realized by crystallographic site engineering, *Chem. Eng. J.*, 2021, **417**, 129224.

18 Y. Yang, Z. Z. Lu, H. Fan, M. H. Chen, L. Shen, X. G. Zhang, Q. Pang, J. H. Chen, P. C. Chen and L. Y. Zhou, Ultra-Broadband Near-Infrared Phosphors Realized by the Heterovalent Substitution Strategy, *Inorg. Chem.*, 2023, **62**, 3601–3608.

19 P. Luo, D. Sun, Z. Lyu, S. Shen, Z. Lu, Z. Li, Z. Yue, C. Lyu and H. You, Highly efficient broadband NIR phosphor $Y_2CaHfScAl_3O_{12}$:Cr^{3+}, Yb^{3+} with superior thermal stability for spectroscopy applications, *J. Mater. Chem. C*, 2023, **11**, 5515–5523.

20 S. Adachi, Photoluminescence spectroscopy and crystal-field parameters of Cr^{3+} ion in red and deep red-emitting phosphors, *ECS J. Solid State Sci. Technol.*, 2019, **8**, R164.

21 G. N. A. De Guzman, M. H. Fang, C. H. Liang, Z. Bao, S. F. Hu and R. S. Liu, Near-infrared phosphors and their full potential: A review on practical applications and future perspectives, *J. Lumin.*, 2020, **219**, 116944.

22 Z. H. Yue, D. S. Sun, Z. Lyu, S. D. Shen, C. Lyu, P. C. Luo and H. P. You, A highly thermally stable $Y_3AlGa_4O_{12}$:Cr^{3+} phosphor for near-infrared pc-LEDs, *J. Mater. Chem. C*, 2023, **11**, 16563–16570.

23 J. Zhu, Z. Xia and Q. Liu, Synthesis and energy transfer studies of $LaMgAl_{11}O_{19}$:Cr^{3+},Nd^{3+} phosphors, *Mater. Res. Bull.*, 2016, **74**, 9–14.

24 G. Liu, T. Hu, M. S. Molokeev and Z. Xia, Li/Na substitution and Yb^{3+} co-doping enabling tunable near-infrared emission in $LiIn_2SbO_6$: Cr^{3+} phosphors for light-emitting diodes, *iScience*, 2021, **24**, 102250.

25 Y. Zhang, S. Miao, Y. Liang, C. Liang, D. Chen, X. Shan, K. Sun and X.-J. Wang, Blue LED-pumped intense short-wave infrared luminescence based on Cr^{3+}-Yb^{3+}-co-doped phosphors, *Light: Sci. Appl.*, 2022, **11**, 136.

26 L. Q. Yao, Q. Y. Shao, S. Y. Han, C. Liang, J. H. He and J. Q. Jiang, Enhancing Near-Infrared Photoluminescence Intensity and Spectral Properties in Yb^{3+} Codoped $LiScP_2O_7$:Cr^{3+}, *Chem. Mater.*, 2020, **32**, 2430–2439.

27 T. Tan, S. W. Wang, J. Y. Su, W. H. Yuan, H. Y. Wu, R. Pang, J. T. Wang, C. Y. Li and H. J. Zhang, Design of a Novel Near-Infrared Luminescence Material $Li_2Mg_3TiO_6$:Cr^{3+} with an Ultrawide Tuning Range Applied to Near-Infrared Light-Emitting Diodes, *ACS Sustainable Chem. Eng.*, 2022, **10**, 3839–3850.

28 C. S. Zhong, Y. H. Xu, X. D. Wu, S. W. Yin, X. B. Zhang, L. Zhou and H. P. You, Near-infrared $Sr_7NaGa(PO_4)_6$:Cr^{3+}, Ln^{3+} (Ln = Nd, Er, and Yb) phosphors with different energy transfer paths: photoluminescence enhancement and versatility, *J. Mater. Chem. C*, 2023, **11**, 3375–3385.

29 T. Z. Wang, Y. Z. Wang, W. B. Chen and Z. G. Xia, Crystallization of $Na_2SrGe_6O_{14}$:Cr^{3+},Yb^{3+} Glass Ceramics Enabling a Watt-Level Output Power NIR-I/NIR-II Lighting Source, *Laser Photonics Rev.*, 2024, **18**, 2300784.

30 D. L. Dexter and J. H. Schulman, Theory Of Concentration Quenching In Inorganic Phosphors, *J. Chem. Phys.*, 1954, **22**, 1063–1070.

31 J. Zhou, Z. Xia, X. Li, X. Yun, J. Sun and D. Xu, A novel near-infrared $LiGaW_2O_8$: Yb^{3+}, Cr^{3+} up-conversion phosphor with enhanced luminescence intensity based on Ho^{3+}/Er^{3+} bridges, *J. Mater. Chem. C*, 2020, **8**, 12189–12195.

32 F. Y. Fan, S. S. Yu, Y. Y. Li, Y. X. Xu, Y. M. Song, H. Y. Wu, W. J. Wang and L. Zhao, Enhancement of the NIR Emission of Cr^{3+}-Yb^{3+} Co-doped $La_3GaGe_5O_{16}$ Phosphors by Doping Nd^{3+} Ions via Efficient Energy Transfer for NIR Spectroscopy Regulation, *Inorg. Chem.*, 2022, **61**, 13618–13626.

33 L. P. Jiang, X. Jiang, J. H. Xie, H. Y. Sun, L. L. Zhang, X. L. Liu, Z. H. Bai, G. C. Lv and Y. J. Su, Ultra-broadband near-infrared $Gd_3MgScGa_2SiO_{12}$: Cr, Yb phosphors: Photoluminescence properties and LED applications, *J. Alloys Compd.*, 2022, **920**, 165912.

34 D. Y. Huang, Q. Y. Ouyang, H. Xiao, B. Wang, H. Z. Lian, Q. G. Zeng and J. Lin, Cr,Yb-codoped $Ca_2LaHf_2Al_3O_{12}$ garnet phosphor: electronic structure, broadband NIR emission and energy transfer properties, *Dalton Trans.*, 2021, **50**, 908–916.

35 Q. Q. Zhang, G. G. Li, P. P. Dang, D. J. Liu, D. Y. Huang, H. Z. Lian and J. Lin, Enhancing and tuning broadband near-infrared (NIR) photoluminescence properties in Cr^{3+}-doped $Ca_2YHf_2Al_3O_{12}$ garnet phosphors via Ce^{3+}/Yb^{3+}-codoping for LED applications, *J. Mater. Chem. C*, 2021, **9**, 4815–4824.

36 R. Shi, S. Miao, X. Lv, D. Chen, Y. Zhang and Y. Liang, High–Efficiency Short–Wave Infrared Emitter Enabled by Cr^{3+}–Yb^{3+} Co–Doped Phosphor, *Adv. Opt. Mater.*, 2024, 2303221.

37 S. Wei, Z. Y. Lyu, D. S. Sun, S. D. Shen, X. W. Zhang, Z. Lu, P. C. Luo, H. Y. Hu and H. P. You, A NIR phosphor with ultra-broadband emission enabled by dual energy transfer within two Cr^{3+} emitters and $Cr^{3+} \rightarrow Yb^{3+}$, *J. Mater. Chem. C*, 2024, **12**, 4977–4985.

38 L. Ma, R. Wei, Q. Yu, P. Dai, X. Tian, F. Hu and H. Guo, Improved broadband luminescence in $Gd_2GaSb_{1-x}Ta_xO_7$: Cr^{3+},Yb^{3+} pyrochlore phosphors: Near-infrared spectroscopic applications and dual-mode optical thermometry, *Mater. Today Chem.*, 2024, **38**, 102090.

39 G. C. Liu and Z. G. Xia, Modulation of Thermally Stable Photoluminescence in Cr^{3+}-Based Near-Infrared Phosphors, *J. Phys. Chem. Lett.*, 2022, **13**, 5001–5008.

40 L. H. Zhou, Z. Y. Lyu, D. S. Sun, S. D. Shen, T. X. Tan, L. X. Wang, H. W. Zhao and H. P. You, Enhanced Thermal Stability and Energy Transfer by Crystal-Field Engineering in a Garnet Phosphor for Thermometry and NIR-LED, *Adv. Opt. Mater.*, 2022, **10**, 2201308.